



A dimensionless analysis to select directed energy deposition process parameters for proper clad formation

Choon Wee Joel Lim^{1,2} · Yanmei Zhang³ · Sheng Huang⁴ · Wai Lee Chan¹

Received: 16 March 2022 / Accepted: 31 October 2022 / Published online: 17 December 2022

© The Author(s), under exclusive licence to Springer-Verlag London Ltd., part of Springer Nature 2022, corrected publication 2022

Abstract

The growing interest in the directed energy deposition process to fabricate and repair thin wall structures has warranted a deeper understanding in the properties of the method's basic building block: clad formation. In this study, clads obtained by depositing stainless steel 316L (SS316L) powder with three different process parameters, namely laser power, laser traverse speed, and powder mass flow rate, were investigated. Repeatability was ensured through a wide sample range per parameter. From the data measurement, the clads have an average hardness close to the typical 200 Hv of SS316L materials, indicating that Hall-Petch effect is dominant. The study also shows that: (i) Laser power is the most significant factor to clad depth, but has little influence on clad thickness. (ii) Laser traverse speed is the dominant parameter to clad height. (iii) Powder mass flow rate tends to compensate depth reduction with thickness gain, resulting in no noticeable effect on clad height. Increasing laser power was observed to be the most effective way to prevent clads from forming with zero dilution, an indicator to how well the printed clad is bonded to the substrate. A dimensionless analysis was derived from the set of SS316L clads. Through validation with different stainless steel datasets and extrapolation to a larger parametric range, the analysis was demonstrated to be able to facilitate the selection of process parameters to meet given requirements on the clad dimensions. As its application is intuitive, the analysis has the potential to be adopted as a standard preprinting tool that will increase success rate, thus improving the manufacturing turnaround time.

Keywords Directed energy deposition · Process parameter selection · Dimensionless analysis · Clad formation · Thin wall structures

1 Introduction

The directed energy deposition (DED) process, classified by ASTM as one of the seven types of additive manufacturing techniques, is adapted from a welding (joining of two metallic parts together) or cladding (coating a thin layer of different metal onto a part) process [1, 2]. These processes typically involve a heat source, such as laser, electron beam, or an arc, which melts either metal powder or wire to form molten droplets that are deposited into a melt pool [3–5]. Other technique, such as cold spray, is classified as a DED process that employs kinetic energy to spray ductile metal onto a surface [3]. Adoption of the DED process for additive

manufacturing sees the changes from a single clad layer to multiple clads printed on top of one another to form a three-dimensional (3D) part. Known for its relatively fast but coarse printing when compared to any powder bed fusion processes, the DED process has seen increased interest over the past years, especially in industries like marine and offshore sectors [6, 7]. However, due to the wide range of materials that these industries utilize, there is a need to characterize the parameters required for the different materials to ensure the proper fusion of metal during the fabrication phase.

There are three different sets of parameters that can influence the DED process: (i) system parameters; (ii) process parameters; and (iii) material parameters. The system parameters are typically set by the manufacturer, including build volume, laser type, laser spot size, and material form such as powder or wire. The process parameters are intrinsic to the system parameters. For example, parameters, such as laser power, laser traverse speed, and powder flow rate, have a maximum operational limit due to system configuration, within which the step size can be defined by the user. Lastly, material parameters

Choon Wee Joel Lim and Wai Lee Chan contributed equally to this work. Choon Wee Joel Lim is currently a senior lead research engineer at Singapore Polytechnic, Department for Technology, Innovation & Enterprise.

✉ Wai Lee Chan
chan.wl@ntu.edu.sg

Extended author information available on the last page of the article.

correspond to both intrinsic and extrinsic properties of the metal used for the DED process. Properties such as melting point, thermal conductivity, and laser absorptivity are intrinsic to the chemical composition of the metal alloy. Examples of extrinsic properties include powder size, shape, and morphology, as well as additives added, such as nucleants to control solidification [8].

When its process parameters used in manufacturing or repair applications are adjusted for different materials, the DED process is able to produce thin-walled parts with high aspect ratio that are otherwise difficult to machine [9]. Furthermore, using a closed-loop control algorithm, Shi and co-workers were able to achieve more than 50% variation in width on both straight and curved thin-walled parts, all maintaining an equal height and comparable microhardness [10].

Another advantage of the DED process is its inherent ability to print new material on any metallic surface, which enables the repairing of parts. However, the performance of the parts after a repair may deteriorate and hence is important to be analyzed. For instance, one study conducted by Sun et al. [11] attempted to repair a T-shaped groove that was machined onto a substrate. The study showed that, with proper parameters, a fine metallurgical bonding between the substrate and repaired zone without any micro-defects can be achieved. Yet, both ductile and brittle fractures were observed in the repaired part, which was attributed to the use of repair material that was slightly different from the substrate during the print. The same study [11] also confirmed that the properties of the repaired part improved with the chemical content of the repair material being closer to that of the substrate. Another study conducted by Kim and Saldana [12] investigated the possibilities of repairs on thin walls using Inconel 625. They varied the process parameter to achieve the desired deposit for the potential of repairing thin wall parts. A thin wall with a layer deposit on top can be akin to a single-track situation.

Other studies conducted in DED research looked at varying the process parameters to obtain certain part properties. By knowing the minimum and maximum processing limits for systems and/or material and narrowing it down to the suitable parameters required, a database for the DED process can be generated. Choi and Chang [13] studied the relationships of laser power, speed, and powder flow rate in terms of their effects on the thickness of printed H13 tool steel. They determined that the feedback control for laser power and layer thickness was strongly affected by the powder flow rate, suggesting that a higher flow rate may lead to more formation of pores and voids. The study by Shah et al. [14] showed that the mean layer height was insensitive to the powder flow rate, but was discernibly affected by the laser power. In contrast, the mean layer width was found to

be more strongly influenced by the powder flow rate than laser power.

The hardness and finishing of a printed part are other metrics that can be used to assess the performance of the print. In the study conducted by Mahamood and Akinlabi [15], a higher scanning speed resulted in a higher hardness of a Ti6Al4V part, which may be attributed to the rapid solidification process that is typically associated with higher scanning speed and tend to induce the hard martensitic formation. At a lower scanning speed, a softer microstructure, known as the Widmanstätten alpha, will form instead, thus reducing the hardness of the part. Regarding the finishing of the clad, Mahamood [16] reported that the cooling-gas rate affected the surface roughness of printed titanium tracks. These studies demonstrate how process parameters, mainly the laser power and gas flow rate, can influence the properties of the prints.

Despite the tremendous efforts that have been invested in studying the DED process, the adoption rate in the industry is generally low for production, which can be attributed to several factors. One of such factors is the difficulty in processing different materials to produce complex parts using commercial DED systems. This situation serves as a huge motivation for this work because, without known process parameters, the development of a new part or the use of a new material can require many iterations, leading to a long turnover time. The overarching goal of this work is to develop a general guideline for the DED process that can be easily adopted for different materials and end products. One aspect to ensure a well-printed part is to understand the formation of the melt pool and clad during the printing process, which generally will be affected by three DED process parameters, namely laser power, powder flow rate, and laser traverse speed.

To study multiple parameters effectively, a typical strategy is to conduct a dimensionless analysis, which has been developed in several studies concerning the selective laser melting (SLM) technique [17–20]. Specifically, Mukherjee and co-workers [18] introduced a non-dimensional lack-of-fusion number and showed its correlation with more common non-dimensional numbers, such as the Marangoni number, which the same group had elaborated in their earlier work [17]. However, as pointed out by Rankouhi et al. [19], the lack-of-fusion number is by no means a simple term to obtain, requiring both experimental and simulation inputs. Instead, Rankouhi et al. [19] derived a more practical non-dimensional number that only requires process parameters that can be obtained prior to printing and can be interpreted as the product of the material's thermophysical properties (i.e., specific heat capacity and heat conductivity), laser volumetric energy density,

and laser dwell time. Coatanéa et al. [20] took the dimensionless analysis even further by combining it with functional modeling to develop parsimonious metrics, which showed promising capabilities for the evaluation of part manufacturability when coupled with singular value decomposition. Though only SLM technology was considered for the proof-of-concept in their work [20], Coatanéa and co-workers were confident that their approach can be extended to other additive manufacturing processes or even the simultaneous integration of several manufacturing techniques.

In the same spirit, the objective of this paper is to apply a practical dimensionless analysis for DED to ensure a successful print. In contrast to SLM, such an effort for DED has not been widely seen. The closest prevailing work is a recent paper by Islam and co-workers [21], which developed and validated a dimensionless number to predict the build height of bulk samples manufactured by the DED technique. The paper paid specific attention to the high-throughput processing of multi-principal element alloys and demonstrated that the dimensionless number can indirectly be used to estimate the cooling rate in the printing of the samples.

The main difference between Ref. [21] and the current study is the latter's emphasis on the industrial applicability of the dimensionless analysis. To ensure that the findings are translational, the current study was conducted with a commercial printer and prealloyed powder to emulate typical industry DED operations. Even under such constraints, this paper confirms the possibility to select process parameters to control the dimensions and quality of a single-track deposition, or a clad, composed of stainless steel powder.

To construct the dimensionless analysis, this paper conducted a 3^3 study (i.e., three settings for three process parameters) on SS316L DED clad, which is a canonical case that will provide intuitive findings on the effects of process parameters. Such a study will be particularly relevant to a thin wall structure with high aspect ratio (i.e., build height to thickness), which can be sensitive to the quality of individual clads that build up the structure. Furthermore, the study can facilitate research on larger prints with geometry that requires zig-zag deposition method and/or utilizes non-linear scans [22].

The remaining of this paper is structured as follows: Details on the SS316L powder and experimental methods used for this study are presented in the next section. Then, the results are discussed in Section 3, starting with separate analyses in terms of the three process parameters before moving on to the development of the dimensionless analysis that study the effects of the parameters combined. Further prints of different stainless steel materials were then printed to verify the dimensionless analysis, followed by

a demonstration of how the analysis should be applied for practical DED operations. Conclusions and future work are provided in Section 4.

2 Materials and methodology

To focus on the development of characterization procedures and facilitate post-printing analyses, stainless steel was chosen to be the feedstock for its quality of reduced risk of hot or solidification cracking during the printing process [23]. Stainless steels also have been prominently researched on [24–26], so this work will have a wide outreach in the additive manufacturing community.

In this study, stainless steel 316L (SS316L) produced by Carpenter Technologies was used, with its chemical composition stated in Table 1. The lower carbon content of 0.03% compared to 0.08% of SS316 ensures better weldability of the metal and ease of achieving a decent melt formation [23, 27]. The powder was atomized using argon gas and is generally of spherical morphology, as seen in the SEM image in Fig. 1. The powder used in this study was further sieved to a particle size that ranges from 45 to 105 μm to achieve an average particle size of 80 μm , which was found to result in better clad formation [28].

All the samples for this work were printed at Nanyang Technological University, Singapore, using the DMG Mori Lasertec 65 3D, a five-axis DED hybrid manufacturing system. This system is equipped with the Laserline LDM diode laser with a wavelength between 960 to 1060 nm and has a maximum output power of 2500 W. The laser beam is transmitted through a Fraunhofer COAX 9 co-axial nozzle with a top hat profile and spot size diameter of 3 mm, according to the manufacturer.

Regarding the selection of parameters in this paper, the default manufacturer's settings were left unchanged with both carrier and shielding gas flow rate at 6 l/min and the nozzle-stand-off distance at 11 mm. The other parameters, laser power, laser traverse speed, and powder flow rate, were varied in accordance with Table 2. The full factorial design of this study was made up of three parameters settings at three levels, constituting 27 different experimental points. Each point was conducted thrice to ensure consistency during data collection, thus generating a total of 81 printed samples. For easy referencing, the experimental points are named with the format of powder flow rate-laser power-traverse speed with the units of g/min, W, and mm/min, respectively. Table 2 shows the full factorial design and the labelling of the various experimental points.

For powder flow rate, the machine only accepts voltage inputs to control the rotation of a disc dispenser within the

Table 1 Element composition of SS316L powder

Element	C	Mn	P	S	Si	Cr	Ni	Mo	N	Fe
%	0.03	2	0.045	0.03	0.75	16-18	10-14	2-3	0.1	Balance

powder hopper, which dispenses the powder. Therefore, the calibration of the powder flow rate had to be performed, as there can be manufacturing deviations in the powder hopper. For example, to achieve a powder flow rate of 14 g/min, the voltage applied to the hopper motor typically ranges from 400 to 500 mV. The powder flow rate was measured with the setup shown in Fig. 2, along with a camera to record the weight increment over a duration of 1 min. Three measurements were made for each voltage setting to calculate a more representative average powder flow rate.

The printing of all 81 SS316L single track clads was conducted on rolled SS316L bars, referred herein as substrate, of size 60 mm (length) × 25 mm (width) × 12 mm (thickness). Each sample is, by design, 50 mm (length) × 3 mm (width) × 1 mm (height), as depicted in Fig. 3. Every sample was printed individually onto its respective substrate with a starting print temperature of approximately 25°C to ensure a fixed initial condition. Printing multiple single tracks on the same substrate may result in a higher starting print temperature for each subsequent track and hence was avoided. Additionally, the substrates were cleaned with isopropyl alcohol prior to printing to remove any residue oil, paint, and debris.

The mass of molten metal deposited onto the substrate was collected by measuring the substrate mass before and after the print. The mass gain due to the molten metal deposition during the printing was compared against the measured powder flow rate input over the duration of the print to determine the efficiency of the printing process, which is given by:

$$\eta_{\text{print}} = \frac{\Delta m_{\text{substrate}}}{\dot{m} \times t} \times 100\% , \quad (1)$$

where \dot{m} is the powder flow rate, t is the print time, and $\Delta m_{\text{substrate}}$ is the change in mass of the substrate due to metal deposition during the printing process.

Similar to cross-section A-A of Fig. 3, all printed samples were sectioned perpendicularly to the laser traverse direction at the center of the printed track. Subsequently, they were mounted in a graphite phenolic resin, ground, polished up to 1 μm, and etched using Kroll's reagent for a duration of 600 s. The etchant would expose the microstructure of both the melt pool and substrate. For electron backscattered detection conducted in a separate study, a better surface finish was required, so the samples of interest were further polished using OPU and OPS to remove and reduce any fine scratches.

All the samples were analyzed by a laser microscope (Keyence VK X250, Japan) and mapped using its proprietary software. Each image was then measured to determine the (i) width, (ii) thickness, (iii) depth, and (iv) total height (the addition of thickness and depth) of the clad. The measurement of both the thickness and depth of the clad was done using the substrate as the reference point, as illustrated in Fig. 4.

For the clad hardness, the samples were tested with the Vickers hardness machine (Future-Tech Microhardness Tester FM-300e) using a load of 300 g. The measurements were carried out at six locations on the cross-section of the clad, as indicated by the × in Fig. 4. The recorded hardness values were averaged to indicate the overall hardness of the clad.

3 Results and discussions

Based on the test scheme given in Table 2, a total of 27 cases, each repeated thrice, were evaluated in this study. The 27 × 3 = 81 clads would provide a distribution of the printing efficiency, clad dimensions, which consist of the width, thickness, depth, and height of the clad (see Fig. 4), and overall clad hardness. The three clads of each case, which were printed with the exact same process parameters, were found to have only minor deviations from each other. Therefore, only the average of each group of three is presented in the following.

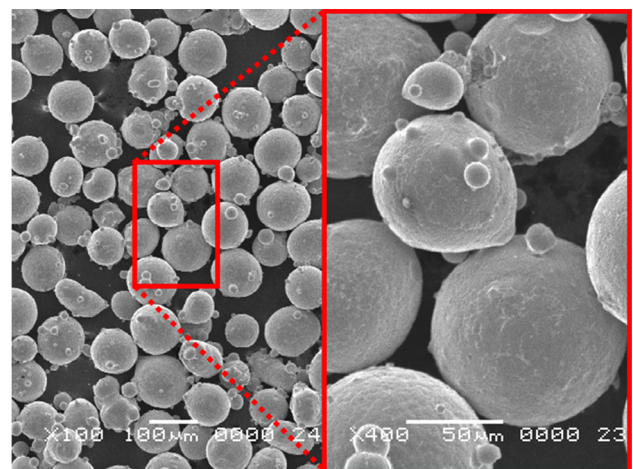


Fig. 1 Illustration of SS316L powder morphology at (a) 100 and (b) 400 magnifications

Table 2 Breakdown of the combinations of process parameters and their nomenclatures

Laser traverse speed		Laser power		
500 mm/min		750 W	1000 W	1250 W
Powder flow rate	10 g/min	10-750-0.5	10-1000-0.5	10-1250-0.5
	12 g/min	12-750-0.5	12-1000-0.5	12-1250-0.5
	14 g/min	14-750-0.5	14-1000-0.5	14-1250-0.5
1000 mm/min		750 W	1000 W	1250 W
Powder flow rate	10 g/min	10-750-1	10-1000-1	10-1250-1
	12 g/min	12-750-1	12-1000-1	12-1250-1
	14 g/min	14-750-1	14-1000-1	14-1250-1
1500 mm/min		750 W	1000 W	1250 W
Powder flow rate	10 g/min	10-750-1.5	10-1000-1.5	10-1250-1.5
	12 g/min	12-750-1.5	12-1000-1.5	12-1250-1.5
	14 g/min	14-750-1.5	14-1000-1.5	14-1250-1.5

3.1 Overall clad formation and relation with linear energy density

During the printing process, cases {10-750-1.5, 12-750-1.5, 14-750-1.5} resulted in balling and the absence of a clad. Upon cooling, the metal “balls” were found to have not bonded with the substrate and fell off easily. An example of such failed prints is shown in Fig. 5(a). Cases {10-750-1, 12-750-1, 14-750-1} also resulted in some balling, but they were found to have bonded with the substrate. Other cases resulted in a well-bonded clad, as shown in Fig. 5(b).

A key metric to define the heating environment [29], which in turn can lead to the balling and failure of clad formation (or lack thereof) is the linear energy density, E :

$$E = \frac{P}{v}, \tag{2}$$

where P is the laser power and v is the laser traverse speed. As shown by (2), the linear energy density is based on the amount of energy given over a certain length of the clad and is independent of powder flow rate. Therefore, the effect of a higher flow rate where more energy is redistributed to melting the incoming powder and less is used to melt the substrate will not be captured by linear energy density [30].

Referring to cases {10-750-1.5, 12-750-1.5, 14-750-1.5}, where both balling and absence of the clad occurred, and cases {10-750-1, 12-750-1, 14-50-1}, where some balling occurred at the sides and the clad just barely bonded, the linear energy density was 30 J/mm and 45 J/mm, respectively. Therefore, one can infer that a lower limit of the linear energy density for the clad to be properly bonded to the substrate exists. Through a parametric search with process parameters not stated in Table 2, this critical linear energy density was found to be 40 J/mm. Note that this value is valid only for the selected machine, printing method, and material chosen for this study and therefore should not be taken as general. The more important



Fig. 2 Powder flow rate measurement setup with a digital weighing scale. A camera was used to record the weight increment over a duration of 1 min. For each voltage input, measurements were conducted thrice to obtain an average powder flow rate output

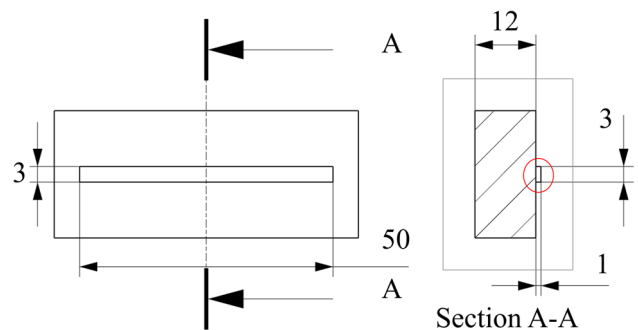


Fig. 3 Schematic illustration of a clad sample as viewed from the (a) top and at the (b) cross-section A-A. All dimensions in mm

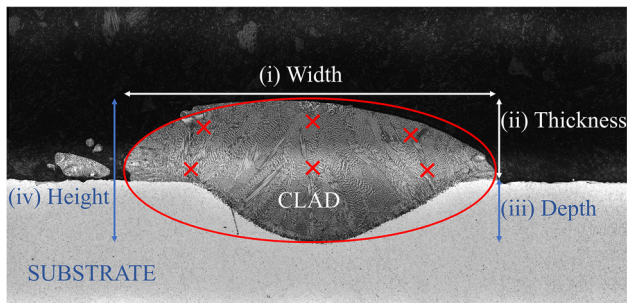


Fig. 4 Definition of the clad dimensions relative to the surface of the substrate. The locations where the hardness test was conducted are marked by \times

takeaway is the existence of a lower limit for the linear energy density.

3.2 Printing efficiency

By its definition in (1), the print efficiency, η_{print} , demonstrates that the process parameters do affect the overall printing efficiency of the system. Generally, it is better to have a higher efficiency to ensure that majority of the powder that is being dispensed into the system forms the clad rather than being blown away or ejected out of the melt pool during printing. However, due to practical reasons, it is impossible to have an efficiency of 100%. On the other hand, poor efficiency due to inappropriate process parameter selection can be costly due to the amount of material wastage. By knowing the efficiency of the selected process parameters, the overall cost of the print can be estimated from the amount of powder used.

Figure 6 depicts the various powder flow rates to the linear energy density and η_{print} , which is defined in (1). For ease of reference, the symbol size scales with the magnitude of the traverse speed, with the largest representing 1500 mm/min. As the linear energy density increases, the spread of the efficiency tends to be smaller, other than an anomaly with a very high efficiency of 85% at $E =$

150 J/mm for powder flow rate $\dot{m} = 10$ g/min. Additionally, the spread tends to reduce in size as the flow rate increases from 10 to 12 g/min and 14 g/min. The trend of the gradient is similar within the same traverse speed group for different powder flow rates. Figure 6 also shows that, with an increase in P/v , the efficiency slope becomes gentler, indicating a drop in the rate of change of efficiency, though always in an increasing direction.

Specifically, cases {10-1250-0.5, 12-1250-0.5, 14-1250-0.5, 12-1250-1.5, 14-1250-1.5} with a higher laser power showed the highest printing efficiency ranging between 70 and 85%. In contrast, samples printed at 750 W resulted in lower efficiency between 50 and 65% in general. The higher printing efficiency from the higher laser power is likely attributed to the availability of energy to melt more powder so that it does not ablate out of the melt pool. Since the efficiency does not tell how well the clad has adhered to the substrate, analysis of the clad cross-section is needed to understand the melt pool formation.

3.3 Vickers hardness measurement

This section will discuss the hardness measured from the 81 experimental samples. Governed by the Hall-Petch effect, where the grain size is a determining factor [31], the expected hardness of SS316L should be within 200 Hv [32]. Post printing, besides the refinement of the grain size through cold working, there is no other mechanism to enhance the hardness of the print [33].

The hardness distribution in Fig. 7 corresponds to the data taken for the 81 samples, each at the six locations illustrated in Fig. 4. Generally, the distribution shows a mean hardness of approximately 200 Hv, agreeing with similar studies [34, 35]. With a standard deviation of 17.55 Hv, the spread of the hardness distribution is reasonable considering that a hardness of 225 Hv has been reported for general additively manufactured SS316L [36]. Likely, the manufacturing technique has some effects on the hardness, though not prominent because of the dominating Hall-Petch effect.



Fig. 5 Example of (a) a poorly bonded melt track and (b) a desirable clad

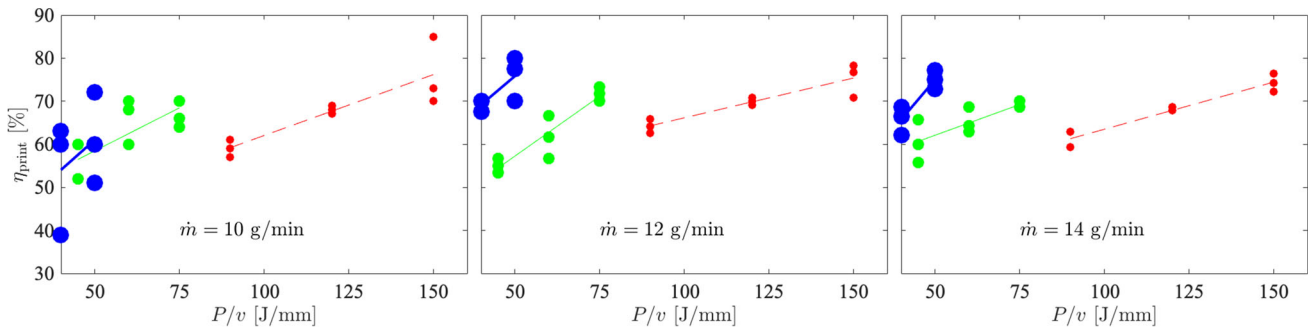


Fig. 6 Printing efficiency, η_{print} , due to variations in linear energy density and powder flow rate. Note that each cluster corresponds to a different laser traverse speed and the size of the symbol scales

with the magnitude of the traverse speed (●: $v = 500$ mm/min, ●: $v = 1000$ mm/min, ●: $v = 1500$ mm/min)

Therefore, Fig. 7 implies that the process parameters have minimal effects on hardness.

3.4 Geometric characterization

The dimensional results of the printed clad samples with variations in the three process parameters will be explored. All 81 clads were first evaluated with respect to laser power, laser traverse speed, and powder flow rate, each at three different levels, using statistical and dimensionless analyses in Sections 3.4.1 and 3.4.2, respectively. Additional clads were printed with stainless steels of different compositions than SS316L to validate the scaling effect in Section 3.4.3. Finally, a demonstration on how the dimensionless analysis can be applied during a practical printing case is presented in Section 3.4.4.

3.4.1 Statistical analysis of clad dimensions and dilution

The plot in Fig. 8 shows the results with the normalized thickness (>0) and depth (<0) in blue and red, respectively, and the error bar is depicted by the black lines. All length scales were normalized by the laser diameter, $D_{\text{laser}} = 3$ mm. From Fig. 8(a), it is discerned that the magnitude

of depth increases as the power increases. At 750 W, no melting of the substrate was observed, resulting in zero depth. Increasing the power to 1000 W resulted in some depth at approximately $-0.03D_{\text{laser}}$. At 1250 W, more depth was obtained at approximately $-0.12D_{\text{laser}}$. These observations show that the melt pool had penetrated the substrate. In contrast, the laser power appears to have small effects on the printed thickness of the clad. Regardless of the power used, there are very little differences in the thickness of the clad, ranging only from 0.2 to 0.23.

The effect of traverse speed on the height of the clad is significant, as shown in Fig. 8(b). As the traverse speed was increased from 500 to 1000 mm/min and then further to 1500 mm/min, the overall height decreased by $>30\%$ and approximately 17%, respectively. The rate of reduction of the magnitude of depth was less than that of thickness, though exhibiting a similar trend. Hence, one may infer that the traverse speed affects the height (depth and thickness combined) most significantly.

In Fig. 8(c), the results reveal that the thickness increases with powder flow rate, whereas the magnitude of depth decreases. In general, a higher powder flow rate would translate to more powder particles being injected into the laser beam, so the energy would be more absorbed by the powders, resulting in less energy for the substrate. Consequently, the clad thickness may increase while the magnitude of depth may decrease. As a result of this countering effect, the powder flow rate did not have a noticeable effect on the overall clad height.

The importance of knowing the dimensions is to determine if the printed clad is well bonded to the substrate, using metrics such as dilution. The definition of dilution depends on the method used to characterize it, which can be through either geometrical or metallurgical means. Studies conducted by Toyserkani et al. and Zhao et al. [37–39] have proposed using the ratio of the volume of the molten substrate to the volume of the deposited layer, which would be accurate, but only feasible if the clad and substrate are

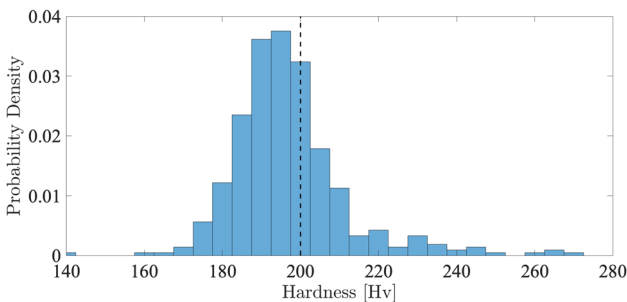


Fig. 7 Distribution of hardness of the 81 experimental samples. Expected hardness for SS316L is 200 Hv [32], which is indicated by the black dashed vertical line

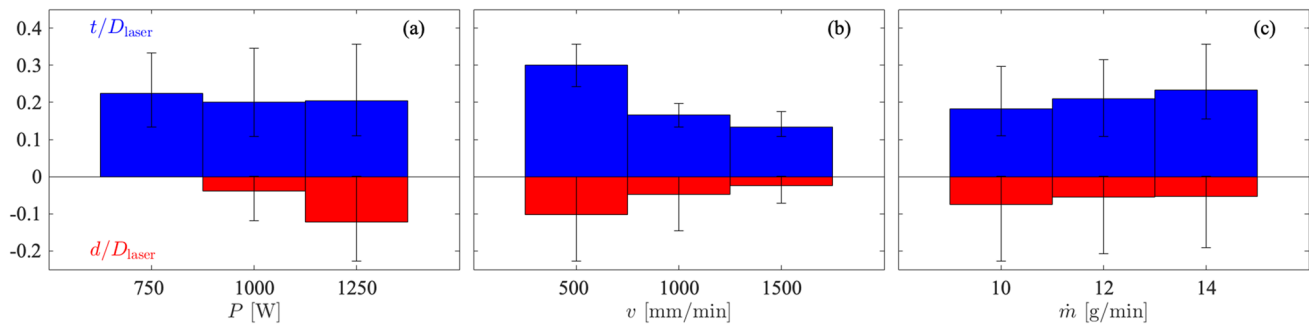


Fig. 8 Histogram of normalised thickness and depth plotted against the three process parameters, (a) laser power, (b) traverse speed, and (c) powder flow rate. The reference length for normalization is the laser diameter, $D_{\text{laser}} = 3 \text{ mm}$

of different materials or if the process is computed in a simulation. Since the clad and substrate in this study are of the same chemical composition, the dilution, δ , was evaluated with the most common method instead, which formulates as [37]:

$$\delta = \frac{d}{d+t}, \quad (3)$$

where d is the depth of the melted clad and t is the thickness of the clad (see Fig. 4). Samples of varying degrees of dilution are depicted in Fig. 9, showing the different types of clad that had been fabricated by varying the process parameters.

Generally, a dilution between 10 and 30% indicates a good melt pool formation [34, 39]. On the one hand, low or no dilution may lead to porosity and air bubbles forming underneath the clad, or poor bonding that results in delamination. On the other, high dilution rates may induce porosity due to keyhole welding effects [40]. Figure 10 describes the distribution of 33 clads (out of the 81 samples) with no dilution and poor adhesion to the substrate. Categorizing these 33 samples under the three parameters shows that the effect of laser power on dilution is the most significant. Specifically, 60% of the clads without dilution corresponds to the low power setting of 750 W. Increasing the laser power reduced the likelihood of no dilution, with the counts dropping to 30% and 10% for 1000 W and 1250 W, respectively.

In contrast, both the traverse speed and powder flow rate do not appear to have any significant effect on the dilution. Within the 33 samples with no dilution, the distribution is generally uniform regardless of the traverse speed and powder flow rate settings. These findings are consistent with the results in Fig. 8, where the laser power was found to yield the most effect on the depth of the clad, since a higher laser power would result in more of the substrate melting.

3.4.2 Dimensionless analysis

In this section, an in-depth evaluation of the effects of the three process parameters on the various dimensions of the clad formation is presented. Note that this study limited the number of process parameters by choice to emulate the typical control one can intuitively exert over a commercial DED printer. If necessary, the analysis can be expanded to include more variables, for instance, hatch spacing and layer thickness. To derive a trend between the geometric variables (i.e., thickness, depth, and width) and the three process parameters (i.e., laser power, laser traverse speed, and powder mass flow rate), a dimensionless analysis based on Buckingham Π theorem [41, 42] was implemented. Samples without dilution were excluded based on the assumption that scaling should only exist for the well-bonded regime. If balling and unbonded clad exist, there is no width or height to evaluate anymore. Additionally, the analysis considers only a nozzle size of approximately

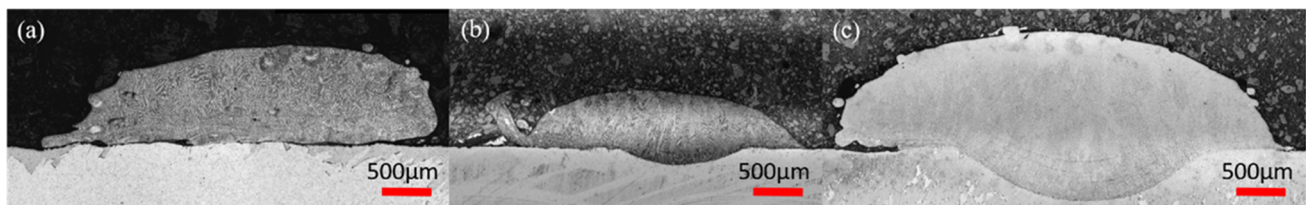


Fig. 9 Center cross-section of three different clad samples: (a) Case 14-750-1 that has no visible dilution. (b) Case 14-1250-1.5 with a small dilution. (c) Case 12-1250-0.5 with good dilution within the recommend range of 10 to 30%

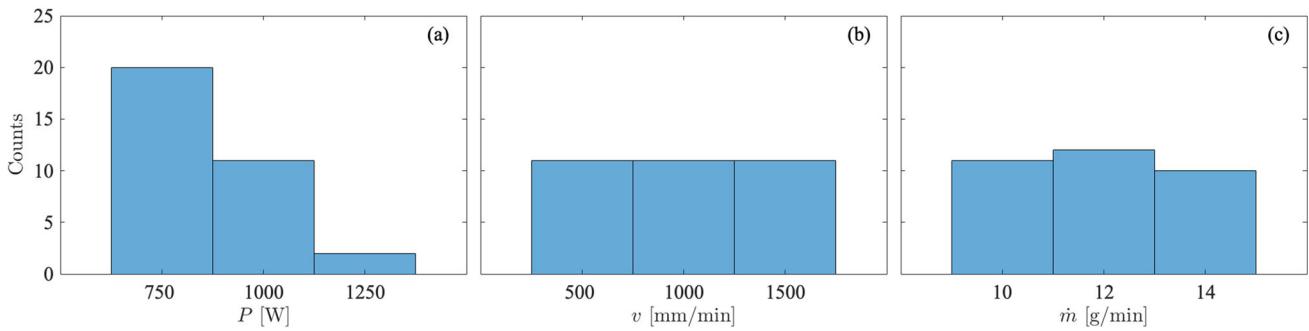


Fig. 10 Distribution of 33 clads with no dilution with respect to the three process parameters, (a) laser power, (b) laser traverse speed, and (c) powder flow rate

3-mm diameter because a variation in the nozzle diameter is not expected to substantially affect the formulation.

The development of the dimensionless analysis is as follows:

- Any one of the clad geometrical dimensions (width, depth, and thickness; see Fig. 4) is assumed to be a function of the process and system parameters. Based on experience, five parameters, namely laser power, P , laser traverse speed, v , powder flow rate, \dot{m} , laser diameter, D_{laser} , and powder melting rate (here specific to SS316L), $\dot{\omega}_{316L}$, were selected due to their typical dominating influence on print dimensions. This assumption is given by:

$$L_{\text{clad}} = f(\underbrace{P, v, \dot{m}}_{\text{Machine}}, \underbrace{D_{\text{laser}}, \dot{\omega}_{316L}}_{\text{Material}}), \tag{4}$$

where L_{clad} is a general notion for any one of the clad dimensions. Note that thermophysical properties of materials have been implicitly included in the powder melting rate term, which can be expanded into:

$$\dot{\omega} = \frac{H_f + c(T_{\text{MP}} - T_{\text{ref}})}{\kappa/\rho c}, \tag{5}$$

where H_f is the latent heat of fusion, c is the specific heat capacity, T_{MP} is the melting temperature, κ is the thermal conductivity, and ρ is the density, all with respect to SS316L in (4). The reference temperature is taken from room condition: $T_{\text{ref}} = 300$ K. Using values from Ref. [43], the powder melting rate can be found as: $\dot{\omega}_{316L} \approx 5 \times 10^{10}$ 1/s.

- The number of non-dimensional variables that can be extracted for this study is given by the difference between the number of dimensional terms (six in (4), including the left-hand-side) and the number of dimensions (three for lengthscale, timescale, and mass, based on the units of the dimensional terms). Therefore, (4) can be rewritten in terms of three non-dimensional terms:

$$L_{\text{clad}}/D_{\text{laser}} = g(\Pi_i, \Pi_{ii}), \tag{6}$$

where the Π terms are not unique and can be made up of any combination of the dimensional parameters stated on the right-hand-side of (4). For a systematic derivation of the dimensionless terms, the readers can refer to the thorough study by Coatanéa et al. [20].

- Here, a suitable set of Π terms and g function was found to be:

$$\Pi_i = \frac{P}{\dot{m}v^2}, \quad \Pi_{ii} = \frac{D_{\text{laser}}\dot{\omega}_{316L}}{v},$$

$$g(\Pi_i, \Pi_{ii}) = h\left(\frac{\Pi_i}{\Pi_{ii}}\right) = h(\Pi_1).$$

Hence, the right-hand-side of (6) can be expressed instead as a function of a single Π_1 term given by:

$$\Pi_1 = \left(\frac{P}{v}\right) \frac{1}{\dot{m}D_{\text{laser}}\dot{\omega}_{316L}}, \tag{7}$$

which can be interpreted as the ratio of laser deposition energy (P/v) to energy needed to melt the metal powder ($\dot{m}D_{\text{laser}}\dot{\omega}_{316L}$), both specific to a linear distance (i.e., per unit length). Equation (7) shows that Π_1 increases as the power increases, or as either powder flow rate or traverse speed decreases, and vice versa.

Interestingly, (7), which is identical to the dimensionless number given in Ref. [21], is similar to the dimensionless number discovered by Rankouhi et al. [19], which pertains to SLM. Specifically, both dimensionless numbers can be factored into two parts, one of which given by the linear energy density (P/v), which was introduced in Section 3.1. The explicit appearance of the linear energy density in both dimensionless numbers explains why the term has typically been regarded as a significant factor of print quality. However, unlike the linear energy density, Π_1 can show the relative effect of all the three process parameters on the dimensions of the clad size.

The difference between the DED and SLM dimension numbers is contained in the other part, $\dot{m}D_{\text{laser}}\dot{\omega}_{316L}$, which is replaced by the ratio of specific heat capacity

to the product of thermal conductivity, laser hatch spacing, and laser scan speed in the SLM study [19]. This similar, but not identical non-dimensional combination of parameters demonstrates the inherent influential elements of laser-based manufacturing techniques, as well as the distinction between two different printing methods.

4. By design, (4) and (6) should hold true for any of the geometrical dimensions. For example:

$$\begin{aligned} d/D_{\text{laser}} &= h(\Pi_1), \quad t/D_{\text{laser}} = h'(\Pi_1), \\ (d+t)/D_{\text{laser}} &= h(\Pi_1) + h'(\Pi_1) \\ &= h''(\Pi_1). \end{aligned} \quad (8)$$

5. Since dilution in this work is defined as the ratio of clad depth to clad height (see (3)), it can be interpreted as the normalized, non-dimensional depth and should also be a function of Π_1 :

$$\begin{aligned} \delta &= \frac{d}{d+t} = \frac{d}{D_{\text{laser}}} \frac{D_{\text{laser}}}{d+t} \\ &= \frac{h(\Pi_1)}{h''(\Pi_1)} = h'''(\Pi_1). \end{aligned} \quad (9)$$

Using the dimensionless analysis, it is possible to generate regions of clads that represent different regimes. Figure 11 is a schematic illustration that sketches three distinct types of clad formation along the characteristic curve given by:

$$\frac{w}{D_{\text{laser}}} = h(\Pi_1).$$

Region 1 on the leftmost portion (i.e., low Π_1) corresponds to clads that will generally not bond properly with the substrate (cf. Figure 5(a)) due to low relative laser power. The region will also exhibit high sensitivity to Π_1 , resulting in steep variation in dilution and clad dimensions with small Π_1 increment as the clad transitions from poor to marginally acceptable bonding with the substrate. Crossing into region 2, which can cover a sizable Π_1 range, the clad formation will stabilize, resulting in a good dilution range that corresponds to a well-bonded clad (see Fig. 5(b)). Because of the stabilization, the deviation in clad dimensions from the characteristic Π_1 curve should be small too, rendering region 2 optimal for quality prints. While the trend should continue into region 3, the associated high relative laser power will likely lead to an excessive melt pool or even keyhole welding. As a result, this high Π_1 zone will possibly be characterized by a wide spread in dilution and clad dimensions, so maintaining a consistent print in region 3 can be challenging. For this reason, along with the corresponding exorbitant laser power that translates to a high cost, region 3 is seldom engaged on purpose in

regular DED operations. Hence, all the 81 clads printed for this study reside only in regions 1 and 2 since there is no practical purpose to expend any resources for region 3, though it should still be assessed in the future for academic interests.

The 48 printed clads with non-zero dilution are plotted with the non-dimensionalized width, w , thickness, t , and depth, d , against Π_1 in the top, middle, and bottom graphs of Fig. 12, respectively. The color scale indicates the linear energy density ranging from 50 to 150 J/mm. Note that the values in the color bar have been normalized by 100 J/mm. Like illustrated in Fig. 11, the width displays a larger variation (up to $0.4D_{\text{laser}}$) for $\Pi_1 \lesssim 3$, but stabilizes into a relatively linear trend (varies within $0.2D_{\text{laser}}$) as Π_1 increases beyond 3. However, the variation in width is not as drastic as portrayed in the schematic diagram, possibly because of the limitation to present only clads with non-zero dilution.

On the other hand, the thickness and depth seem to have less deviations than the width, likely due to the lower magnitude of the two variables (within $0.3D_{\text{laser}}$, while the width can reach D_{laser}). Overall, all three dimensions can apparently be fitted reasonably by a first-order polynomial line with respect to Π_1 . The resulting best fit lines can be expressed as:

$$\frac{w}{D_{\text{laser}}} = 0.0522\Pi_1 + 0.744, \quad (10a)$$

$$\frac{t}{D_{\text{laser}}} = 0.0423\Pi_1 + 0.083, \quad (10b)$$

$$\frac{d}{D_{\text{laser}}} = 0.0360\Pi_1 - 0.012, \quad (10c)$$

and are indicated by a solid red line in Fig. 12.

Regions 1 and 2 are more clearly demarcated by plotting dilution, $\delta = d/(d+t)$, against Π_1 , as shown in Fig. 13, where the shaded grey region indicates the recommended dilution range of 10 to 30% for a good melt pool formation [34, 39]. On the left of Fig. 13, where Π_1 is low, region 1 shows clads with a large variation in dilution (approximately 0 to 0.5) for a range of $\Pi_1 = [1.5, 3]$. This cluster contains clads of low height, some of which with dilution close to 0, indicating that the clads in region 1 are typically flat and not well-bonded to the substrate, like the inset for region 1 in Fig. 11. Therefore, for the sake of determining a suitable set of process parameters for a successful print, region 1 should be avoided as the clads printed may be of poorer quality. This exclusion effectively means that the setting of process parameters that results in low Π_1 value is generally not recommended.

As compared to region 1, region 2 has a more stable dilution with less variations with respect to Π_1 value, ranging from 10 to 50% for $\Pi_1 = [3.5, 6]$ in accordance

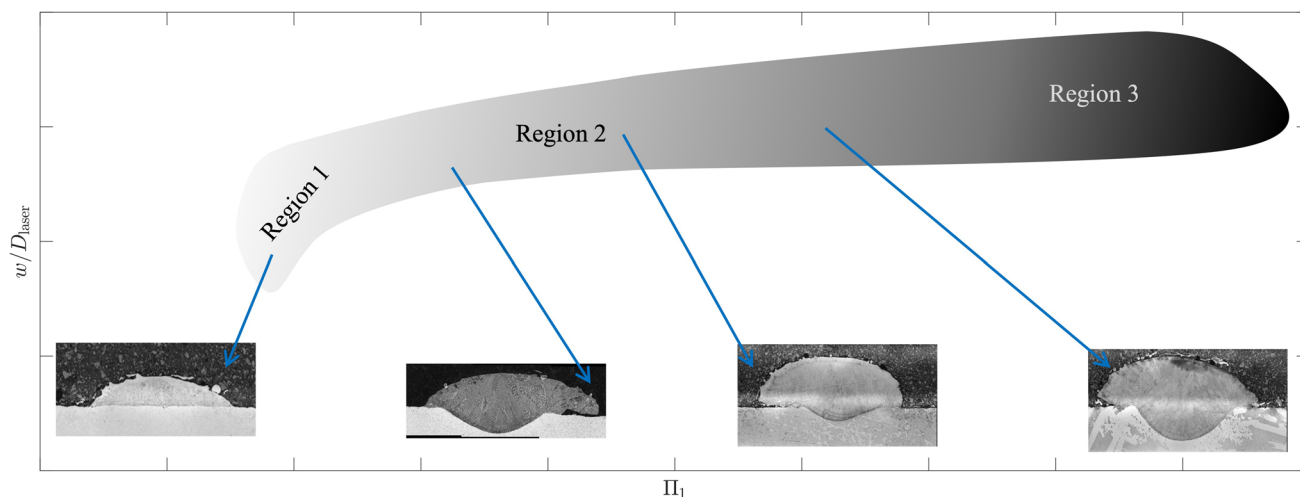


Fig. 11 Schematic illustration of the non-dimensional width, plotted against the non-dimensional Π_1 term, which will reveal three general regions of clad formation. Center cross-sections representative of regions 1 and 2 and different clad height are shown by the insets. The

insets show a possible trend of clad formation that should stabilize around the range of Π_1 in region 2. More spread and growth in the clad width will be expected when crossing into region 3

with Fig. 13. These clads were generally well-bonded due to sufficient melting of both powder and substrate.

The two clusters of dilution scatter denoting regions 1 and 2 in Fig. 13 indicate a discontinuity as Π_1 increases from 3 to 3.5. In contrast, the width, thickness, and depth scatters in Fig. 12 appear to be more continuous with Π_1 .

Combining all the findings so far, a reasonable inference for applications concerning DED of SS316L parts will be

to operate with a combination of process parameters that corresponds to region 2. Here, this particular region was found to correspond to $\Pi_1 > 3$, and is analogous to the process windows that are suggested in previous studies for metal powder bed additive manufacturing [19, 45]. Interestingly, the presented empirical observations appear to be supported by numerical results of the same Π_1 range as well. The simulations, performed by Zhang et al. [44], are

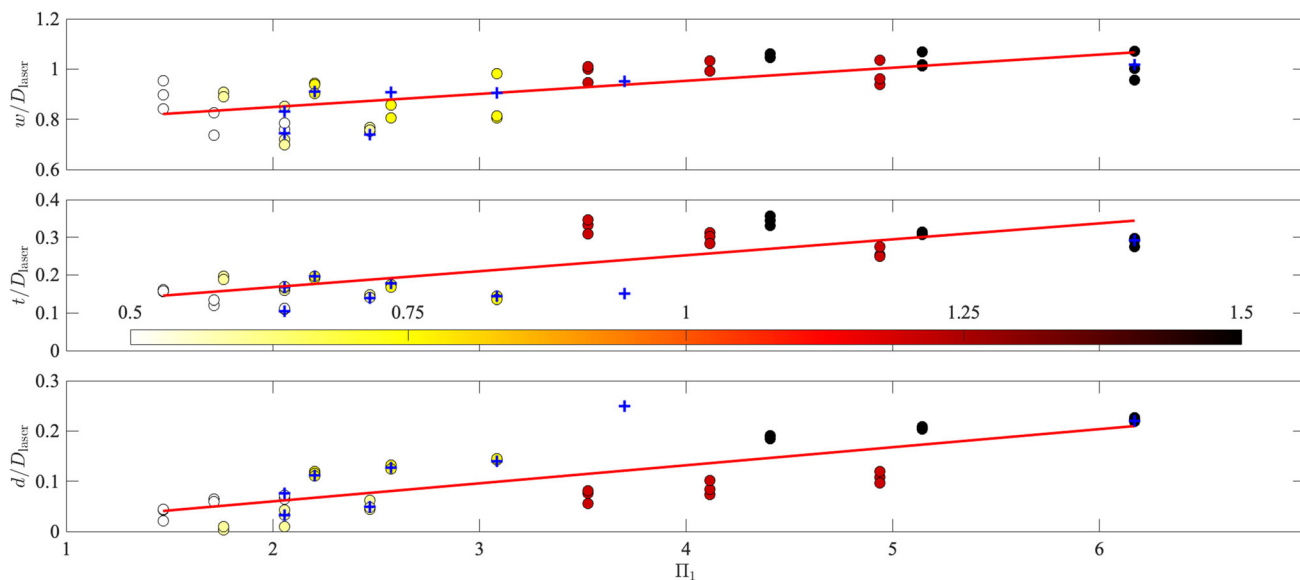


Fig. 12 Non-dimensional width (top), thickness (middle), and depth (bottom) plotted against non-dimensional parameter, Π_1 (see (7)). \circ denotes the 48 samples (out of 81 samples) with dilution > 0 and $+$ indicates the simulation results from Ref. [44]. The sample points are

colored by the linear energy density, P/v , normalized by 100 J/mm. Overall, the three clad dimensions appear to be reasonably fitted by a first-order polynomial line with respect to Π_1 . The expressions for the three best fit lines, denoted by a solid red line, are given in (10)

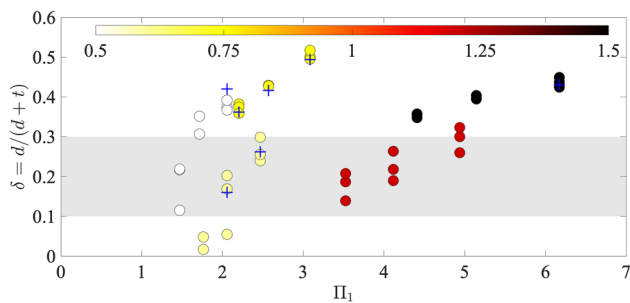


Fig. 13 Clad dilution plotted against the non-dimensional parameter, Π_1 (cf. (7)). The shaded grey region indicates the recommended dilution range of 10 to 30% [34, 39]. Refer to Fig. 12 for further details on the remaining notations of this plot. Similar to the schematic illustration in Fig. 11, two regions can be seen, separated discontinuously at approximately $\Pi_1 = 3$. Large variation in dilution is first observed at lower Π_1 , which reduces to smaller deviations as Π_1 increases beyond 3

denoted by + in Figs. 12 and 13, where good agreement with the measured w , t , d , their respective best fit lines, and δ can generally be seen.

3.4.3 Validation of dimensionless analysis

Validation of the dimensionless analysis based on Buckingham Π theorem was conducted to ensure that the scaling with non-dimensional clad width, thickness, and depth and the non-dimensional parameter, Π_1 , which denotes the ratio of laser deposition energy to the energy needed to melt the metal powder (see Section 3.4.2 for derivation), indeed applies. To do so, 48 additional clads, one half with Uddeholm Corrax [46] and the other with BÖHLER M789 AMPO [47], were printed with different sets of process parameters that cover a range of $\Pi_1 = [1, 18]$. Corrax and M789 are specialized stainless mold steel and maraging steel, respectively. While still belonging to the class of steel, Corrax and M789 will display different behaviors from each other, as well as from SS316L due to the differences in their element composition (see Tables 1 and 3). Similar to the analysis performed on the 81 SS316L clads in the preceding section, the clad width, thickness, and depth were measured for each prescribed Π_1 value. These measured data will be referred as the “Actual” results.

From the SS316L dataset evaluated in Section 3.4.2, best fit lines of first-order polynomial with respect to Π_1

have been extracted for the non-dimensional clad width, thickness, and depth. Using the best fit lines’ expressions shown in (10) and given Π_1 , the clad characteristic lengths can be predicted. The dilution can be further determined since it is defined in (3) as the ratio of depth to the sum of depth and thickness. Note that the best fit lines were derived from a range of Π_1 up to 6 (see Fig. 12), so some of the calculations here are extrapolation rather than interpolation, thus truly challenging the applicability of the dimensionless analysis. These predicted data will be labelled as the “Calculated” results.

The comparison of the actual and calculated non-dimensional clad width, w , thickness, t , and depth, d , is given in left, center, and right correlation plots of Fig. 14, respectively. Unlike Figs. 12 and 13, the color scale here indicates the magnitude of Π_1 , so a different color scheme was used. The datapoints of Corrax and M789 are denoted by square and diamond symbols, respectively. Except for clad thickness, the calculated clad dimensions appear to agree reasonably with their actual counterparts. Specifically, both the clad width and depth of Corrax show a correlation of more than 80%, while that of M789 display correlation of 73% and 66%, respectively.

For clad thickness, the actual and calculated results generally match better for the lower $\Pi_1 < 10$ range. As Π_1 increases, the fitting begins to overpredict the clad thickness. Recall that the best fit lines were extracted from a range of $\Pi_1 = [1, 6]$, such a discrepancy is not unexpected and suggests that, for thickness: (i) a larger Π_1 range than that evaluated in Section 3.4.2 is needed to better represent Region 2; and (ii) the model may require a higher-order polynomial function. Despite its incompatibility with the higher Π_1 range, the thickness fitting still returns a good correlation of approximately 90% when the evaluation is limited to datapoints that correspond to $\Pi_1 < 10$.

The dilution of the Corrax and M789 clads is plotted against Π_1 in Fig. 15, along with that of SS316L from Fig. 13, repeated here for reference. Note that the color range in Fig. 15 has been shifted to account for the larger range of linear energy density that has been covered in this validation study. Like in Fig. 14, the points of Corrax and M789 are denoted here by square and diamond, respectively.

Even with the additional information from the Corrax and M789 clads, the discontinuous separation of regions 1 and 2 is still apparent in Fig. 15. However, instead of

Table 3 Element composition of Uddeholm Corrax and BÖHLER M789 AMPO powders [46, 47]

Element	C	Mn	Si	Cr	Ni	Mo	Ti	Al	Fe
Corrax (%)	0.03	0.3	0.3	12	9.2	1.4	0	0	Balance
M789 (%)	0	0	0	12.2	10.0	1.0	1.0	0.6	Balance

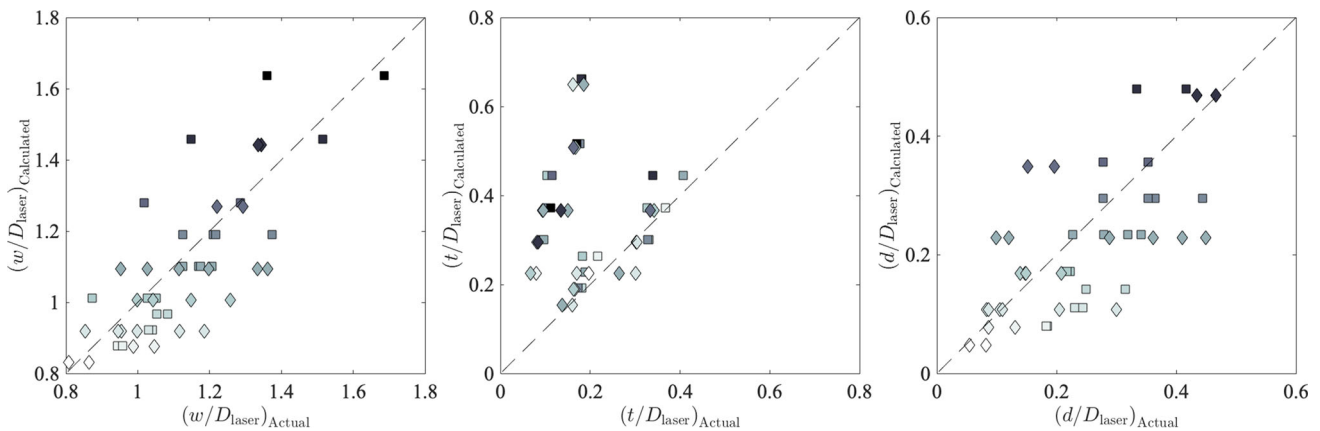


Fig. 14 Correlation plots for measured (Actual) and predicted (Calculated; based on (10)) non-dimensional clad width (left), thickness (center), and depth (right). The sample points of Corrax and M789 are differentiated by square and diamond symbols, respectively, and are

colored by the non-dimensional parameter, Π_1 , which ranges from 1 to 18 here. The correlation is reasonably good (i.e., generally more than 70%) for width and depth. For thickness, the correlation is only satisfactory when limited to the $\Pi_1 < 10$ range

a vertical cutoff as postulated in Section 3.4.2, the gap appears to be described by $0.025\Pi_1 + 0.3$, where $\Pi_1 > 3$. Correspondingly, regions 1 and 2 overlap over a range of $\Pi_1 = [3, 9]$ here. The cause of the switch from region 1 to 2 is beyond the scope of this paper, but should be an important mechanism to explore in future studies. These differences also reiterate the importance to progressively expand the parametric space of the dimensionless analysis for a better representation of the clad characteristic lengths.

Overall, this validation study presents a reasonably good agreement between the actual and predicted clad characteristic lengths, even when the best fit models were applied to different stainless steels and extrapolated to larger Π_1 . Hence, the dimensionless analysis developed in Section 3.4.2 is validated and seemingly general to most steel-based powders.

3.4.4 Application of dimensionless analysis

This section presents how the dimensionless analysis is envisioned to be applied in the practical DED processes. Listed in the following are the various key steps:

1. Clad information should be collected before printing to construct the characteristic lines as shown in Fig. 12.
2. Based on user’s needs, a set of width, thickness, and depth can be prescribed, while the dilution can be estimated.
3. Then, from Fig. 12, or equivalently Fig. 13, the corresponding non-dimensional parameter, Π_1 , can be derived.
4. With Π_1 known and given laser spot size and thermochemical properties of the prealloyed powder, the three

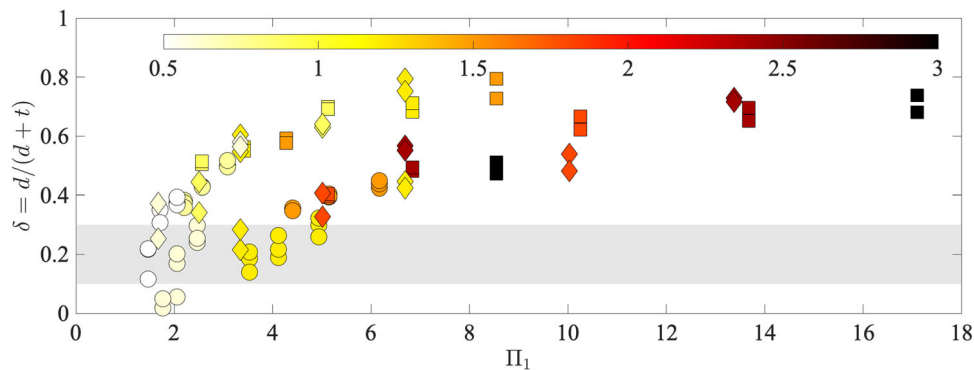


Fig. 15 Clad dilution of SS316L (circle), Corrax (square), and M789 (diamond) plotted against the non-dimensional parameter, Π_1 . The shaded grey region indicates the recommended dilution range of 10 to 30% [34, 39]. The sample points are colored by the linear energy

density, P/v , normalized by 100 J/mm. Note the difference in color range from Fig. 13 due to the larger range of linear energy density covered here. Like before, two regions that are separated discontinuously can be observed, with regions 1 and 2 overlapping over $\Pi_1 = [3, 9]$

Table 4 Tabulation of expected and measured clad width, thickness, and depth for Π_1 of 3 and 4.3, each with three clads printed

		Measured		
$\Pi_1 = 3$	Expected	Clad 1	Clad 2	Clad 3
	w/D_{laser}	0.902	0.883	0.930
	t/D_{laser}	0.211	0.189	0.202
	d/D_{laser}	0.097	0.096	0.103
$\Pi_1 = 4.3$	Expected	Clad 1	Clad 2	Clad 3
	w/D_{laser}	0.971	0.954	0.940
	t/D_{laser}	0.267	0.258	0.261
	d/D_{laser}	0.143	0.160	0.143

process parameters, namely laser power, traverse speed, and powder flow rate, can be set accordingly using (7).

Consider the following application with SS316L powder and a commercial DED printer: The clad needed is of $0.9D_{\text{laser}}$ wide, $0.2D_{\text{laser}}$ thick, and $0.1D_{\text{laser}}$ deep. From Fig. 12, the corresponding Π_1 for this application is approximately 3. Recognizing the industry's emphasis in high-throughput rate, maximizing laser traverse speed is arguably the logical choice. Supposed the printer has a maximum laser power of 1200 W and small powder mass flow rate variations about 12 g/min, the highest traverse speed will then approximately be 816 mm/min.

Another scenario may see the user requiring a clad with larger width, thickness, and depth of D_{laser} , $0.3D_{\text{laser}}$, and $0.15D_{\text{laser}}$, respectively, thus necessitating a larger Π_1 of approximately 4.3. Assuming that the printer in this case is limited to a maximum traverse speed of 616 mm/min and fixed powder mass flow rate of 12 g/min, the corresponding laser power will then approximately be given by 1300 W.

For each of the two cases, three SS316L clads were printed using the aforementioned settings. The measured characteristic lengths of the six SS316L clads are tabulated in Table 4. The mean errors in clad width, thickness, and depth are illustrated in Fig. 16, all within a 10% range, thus

confirming once again the applicability of the dimensionless analysis developed in Section 3.4.2. More importantly, this demonstration shows how the dimensionless analysis can be intuitively applied and hence has the potential to be adopted by the DED community as a standard tool.

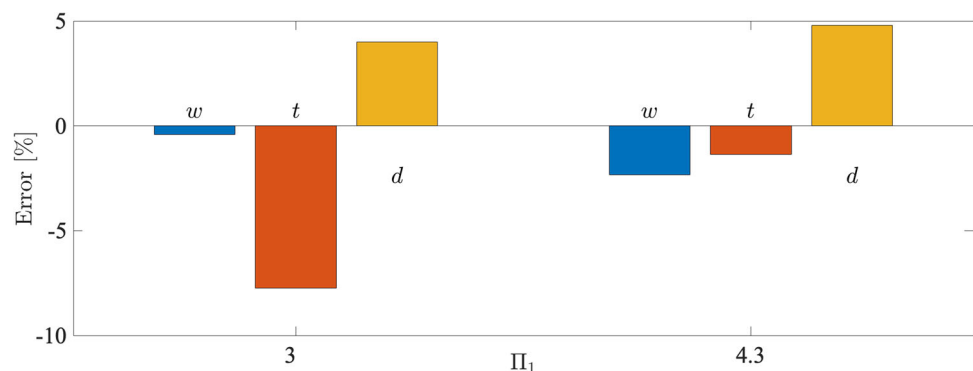
4 Conclusions

In this paper, the characterization of single-track laser deposited stainless steel clad was performed using a dimensionless analysis derived for the DED process. Recognizing the importance for industry adoption, the analysis had placed specific emphasis in using only parameters that are available on commercial printers and can be prescribed before printing, along with prealloyed powder so that the thermochemical properties are fixed, thus keeping the analysis as simple for implementation as possible. The study was constructed with 81 clad samples, with repeatability ensured through a wide sample range per parameter. A dimensionless parameter, identical to that in a previous study [21], was found and verified with further experiments. The application of the dimensionless analysis for practical DED operations was demonstrated through explicit examples.

Major findings from this study are as follows:

- SS316L clads printed with the DED technique can be classified by the clad dimensions and hardness of the cross-section of each clad.
- Hardness of SS316L DED tracks generally averages around 180 Hv to 220 Hv, which is close to the typical SS316L hardness of 200 Hv. The mild influence from the manufacturing technique is attributed to the Hall-Petch effect where the material hardness is determined by its grain size.
- The most significant parameter for clad depth is laser power due to its huge impact on the melt pool formation. However, laser power appears to have little influence on the clad thickness.

Fig. 16 Percentage error between expected and measured clad width, thickness, and depth for Π_1 of 3 and 4.3, averaged over the three clads printed for each Π_1 case



- The dominant parameter in determining the overall clad height of the part is the laser traverse speed. Increment in the traverse speed will result in a lower clad height and vice versa.
- Higher laser power seems to reduce the likelihood of clads being formed with zero dilution. Such an effect on the dilution was not observed for both traverse speed and powder flow rate.
- The dimensionless parameter for DED clads can be interpreted as the ratio of laser deposition energy to the energy needed to melt the metal powder. Best fit lines of first-order polynomial functions with respect to the dimensionless parameter were extracted from the SS316L dataset and verified by reasonable agreement attained in applications to stainless mold steel and maraging steel.

Future work can consider applying the clad models to predict and quality control thin wall structures from DED process. Extension of the analysis to materials other than stainless steels and, as suggested by Coatanéa et al.[20], an integration with other additive or even traditional manufacturing techniques will test the generality of the dimensionless analysis. The analysis can also be useful in providing constraints to guide real-time monitoring [48] or control algorithms [10] that can enhance the quality of parts manufactured by the DED process.

Acknowledgements This research is supported by the National Research Foundation, Prime Minister's Office, Singapore, under its Medium Sized Centre funding scheme. The authors acknowledge supports from the School of Mechanical and Aerospace Engineering and Singapore Centre for 3D Printing (SC3DP), Nanyang Technological University, Singapore, and the National Additive Manufacturing Innovation Cluster (NAMIC), Singapore.

Author contribution Conceptualization, experimental investigation, and data collection were performed by Choon Wee Joel Lim. Development of methodology, validation, and data analysis and visualization were conducted by Choon Wee Joel Lim and Wai Lee Chan. The first draft of the manuscript was written by Choon Wee Joel Lim. All authors contributed to reviewing and editing of the subsequent versions of the manuscript. All authors read and approved the final manuscript.

Data Availability The data that support the findings of this study are available from Wai Lee Chan upon reasonable request.

References

1. Wohlers TT, Ian C, Olaf D, Joseph K (2018) Wohlers report 2018 Wohlers Associate Inc
2. ASTM International (2015) ISO/ASTM52900-15, Standard Terminology for additive manufacturing - General principles - Terminology. ASTM International, West Conshohocken PA
3. Dass A, Moridi A (2019) State of the art in directed energy deposition: from additive manufacturing to materials design. *Coatings* 9(418)
4. Thompson SM, Bian L, Shamsaei N, Yadollahi A (2015) An overview of direct laser deposition for additive manufacturing; Part I: Transport phenomena, modeling and diagnostics. *Addit Manuf* 8:36–62
5. Shamsaei N, Yadollahi A, Bian L, Thompson SM (2015) An overview of direct laser deposition for additive manufacturing; Part II: Mechanical behavior, process parameter optimization and control. *Addit Manuf* 8:12–35
6. Williams SW, Martina F, Addison AC, Ding J, Pardal G, Colegrove P (2016) Wire+ arc additive manufacturing. *Mater Sci Technol* 32(7):641–647
7. Ding D, Pan Z, Cuiuri D, Li H (2015) A multi-bead overlapping model for robotic wire and arc additive manufacturing (WAAM). *Rob Comput Integr Manuf* 31:101–110
8. Martin JH, Yahata BD, Hundley JM, Mayer JA, Schaedler TA, Pollock TM (2017) 3D printing of high-strength aluminium alloys. *Nature* 549(7672):365–369
9. Atwood C, Ensz M, Greene D, Griffith M, Harwell L, Reckaway D, Romero T, Schlienger E, Smugeresky J (1998) Laser engineered net shaping (LENS(TM)): a tool for direct fabrication of metal parts. Paper presented at the 17th international congress on applications of lasers and electro-optics, Orlando, FL: SAND98-2473C
10. Shi TBL, Shen T, Zhang R, Shi S, Fu G (2018) Closed-loop control of variable width deposition in laser metal deposition. *Int J Adv Manuf Technol* 97:4167–4178
11. Sun GF, Shen XT, Wang ZD, Zhan MJ, Yao S, Zhou R, Ni ZH (2019) Laser metal deposition as repair technology for 316L stainless steel: influence of feeding powder compositions on microstructure and mechanical properties. *Opt Laser Technol* 109:71–83
12. Kim MJ, Saldana C (2020) Thin wall deposition of IN625 using directed energy deposition. *J Manuf Processes* 56:1366–1373
13. Choi J, Chang Y (2005) Characteristics of laser aided direct metal/material deposition process for tool steel. *Int J Mach Tools Manuf* 45:597–607
14. Shah K, Haq IU, Khan A, Shah SA, Khan M, Pinkerton AJ (2014) Parametric study of development of inconel-steel functionally graded materials by laser direct metal deposition. *Mater Des* 54:531–538
15. Mahamood RM, Akinlabi ET (2017) Scanning speed influence on the microstructure and micro hardness properties of titanium alloy produced by laser metal deposition process. *Mater Today Proc* 4(4):5206–5214
16. Mahamood RM (2018) Effect of laser power and gas flow rate on properties of directed energy deposition of titanium alloy. *Lasers Manuf Mater Process* 5(1):42–52
17. Mukherjee T, Manvatkar V, De A, DebRoy T (2017) Dimensionless numbers in additive manufacturing. *J Appl Phys* 121(064904)
18. Mukherjee T, DebRoy T (2018) Mitigation of lack of fusion defects in powder bed fusion additive manufacturing. *J Manuf Processes* 36:442–449
19. Rankouhi B, Agrawal AK, Pfefferkorn FE, Thoma DJ (2021) A dimensionless number for predicting universal processing parameter boundaries in metal powder bed additive manufacturing. *Manuf Lett* 27:13–17
20. Coatanéa E., Nagarajan HPN, Panicker S, Prod'hon R, Mokhtarian H, Chakraborti A, Paris H, Ituarte IF, Haapala KR (2021) Systematic manufacturability evaluation using dimensionless

- metrics and singular value decomposition: a case study for additive manufacturing. *Int J Adv Manuf Technol* 115:715–731
21. Islam Z, Nelaturu P, Thoma DJ (2021) A dimensionless number for high-throughput design of multi-principal element alloys in directed energy deposition. *Appl Phys Lett* 119:231901
 22. Wong CH, Lim CWJ (2018) Investigation of effects of printing patterns on geometry and densification of stainless steel 316L through directed energy deposition. Paper presented at the 3rd international conference on progress in additive manufacturing (Pro-AM 2018)
 23. Lippold JC, Kotecki DJ (2005) *Welding metallurgy and weldability of stainless steels*. Wiley, New York
 24. Bayode A, Pityana S, Titilayo Akinlabi E (2018) Fabrication of stainless steel based fgm by laser metal deposition. In: Kumar K, Paulo Davim J (eds) *Hierarchical composite materials*. De Gruyter, pp 55–72
 25. Zhang K, Wang S, Liu W, Shang X (2014) Characterization of stainless steel parts by laser metal deposition shaping. *Mater Des* 55:104–119
 26. Chen X, Li J, Cheng X, He B, Wang H, Huang Z (2017) Microstructure and mechanical properties of the austenitic stainless steel 316L fabricated by gas metal arc additive manufacturing. *Mater Sci Eng A* 703:567–577
 27. McHone Industries (2018) Inc.: 316 vs 316L stainless steel: what's the difference? Available at: <https://blog.mchoneind.com/blog/316-vs-316l-stainless-steel> Last Accessed: 11/12/2019
 28. Kong CY, Carroll PA, Brown P, Scudamore RJ (2007) The effect of average powder particle size on deposition efficiency, deposit height and surface roughness in the direct metal laser deposition process. Paper presented at the 14th International Conference on Joining of Materials
 29. Yakout M, Cadamuro A, Elbestawi MA, Veldhuis SC (2017) The selection of process parameters in additive manufacturing for aerospace alloys. *Int J Adv Manuf Technol* 92:2081–2098
 30. Gedda H, Powell J, Wahlström G, Li WB, Engström H, Magnusson C (2002) Energy redistribution during CO₂ laser cladding. *J Laser Appl* 14(2):78–82
 31. Singh KK, Sangal S, Murty GS (2002) Hall-petch behavior of 316L austenitic stainless steel at room temperature. *Mater Sci Technol* 18:165–172
 32. Muthukumar V, Selladurai V, Nandhakumar S, Mouleeswaran S (2010) Experimental investigation on corrosion and hardness of ion implanted aisi 316l stainless steel. *Mater Des* 31:2813–2817
 33. McGuire MF (2008) *Stainless steels for design engineers*. ASM International
 34. Mazzucato F, Aversa A, Doglione R, Biamino S, Valente A, Lombardi M (2019) Influence of process parameters and deposition strategy on laser metal deposition of 316L powder. *Metals* 9(11):1160
 35. Mahmood K, Pinkerton AJ (2013) Direct laser deposition with different types of 316l steel particle: a comparative study of final part properties. In: *Proc Inst Mech Eng Part B: J Eng Manuf*. vol 227, pp 520–531
 36. Zuback JS, DebRoy T (2018) The hardness of additively manufactured alloys. *Materials* 11(11):2070
 37. Toyserkani E, Khajepour A, Corbin SF (2004) *Laser cladding*. CRC Press
 38. Zhao G, Cho C, Kim J.-D. (2003) Application of 3D finite element method using Lagrangian formulation to dilution control in laser cladding process. *Int J Mech Sci* 45(5):777–796
 39. Ramasubbu V, Chakraborty G, Albert SK, Bhaduri AK (2011) Effect of dilution on GTAW colmonoy 6 (AWS NiCr – C) hardface deposit made on 316LN stainless steel. *Mater Sci Technol* 27(2):573–580
 40. Nishimoto K, Mori H (2004) Hot cracking susceptibility in laser weld metal of high nitrogen stainless steels. *Sci Technol Adv Mater* 5(1–2):231–240
 41. Sonin AA (2004) A generalization of the π -theorem and dimensional analysis. *Proc Natl Acad Sci* 101(23):8525–8526
 42. Buckingham E (1914) On physically similar systems; Illustrations of the use of dimensional equations. *Phys Rev* 4(4):345–376
 43. Cervera F (2002) ASMIMPD Committee: ASM ready reference, thermal properties of Metals. ASM International
 44. Zhang Y, Lim CWJ, Tang C, Li B (2021) Numerical investigation on heat transfer of melt pool and clad generation in directed energy deposition of stainless steel. *Int J Therm Sci* 165:106954
 45. Gordon JV, SP N, Cunningham RW, Liu H, Chen H, Suter RM, Beuth JL, Rollett AD (2020) Defect structure process maps for laser powder bed fusion additive manufacturing. *Addit Manuf* 36:101552
 46. Uddeholms AB (2016) Uddeholm Corrax®. Ed. 9, available at https://www.uddeholm.com/files/PB_Uddeholm_corrax_english.pdf
 47. Voestalpine Böhler Edelstahl GmbH & Co KG: BÖHLER Additive Manufacturing Powder: M789 AMPO/Fe-Based Alloys (2022). Available at <https://www.boehler-edelstahl.com/app/uploads/sites/92/2022/06/productdb/api/m789-ampo.en.pdf>
 48. Liu Y, Wang L, Brandt M (2021) An accurate and real-time melt pool dimension measurement method for laser direct metal deposition. *Int J Adv Manuf Technol* 114:2421–2432

Publisher's note Springer Nature remains neutral with regard to jurisdictional claims in published maps and institutional affiliations.

Springer Nature or its licensor (e.g. a society or other partner) holds exclusive rights to this article under a publishing agreement with the author(s) or other rightsholder(s); author self-archiving of the accepted manuscript version of this article is solely governed by the terms of such publishing agreement and applicable law.

Affiliations

Choon Wee Joel Lim^{1,2}  · Yanmei Zhang³  · Sheng Huang⁴  · Wai Lee Chan¹ 

Choon Wee Joel Lim
CLIM065@e.ntu.edu.sg

Yanmei Zhang
zhangym@cqu.edu.cn

Sheng Huang
sheng007@e.ntu.edu.sg

- ¹ School of Mechanical and Aerospace Engineering, Singapore Center for 3D Printing, Nanyang Technological University, Singapore, 50 Nanyang Avenue, S(639798), Singapore, Singapore
- ² National Additive Manufacturing Innovation Cluster, Nanyang Technological University, Singapore, 50 Nanyang Avenue, S(639798), Singapore, Singapore
- ³ College of Aerospace Engineering, Chongqing University, 174 Shazhengjie, Shapingba, Chongqing, 400044, China
- ⁴ School of Mechanical and Aerospace Engineering, Nanyang Technological University, Singapore, 50 Nanyang Avenue, S(639798), Singapore, Singapore